Derivative-based image quality measure for autofocus in electron microscopy

EINDHOVEN UNIVERSITY OF TECHNOLOGY
Department of Mathematics and Computer Science

CASA-Report 10-42
July 2010

Derivative-based image quality measure

by

M.E. Rudnaya, R.M.M. Mattheij, J.M.L. Maubach

Centre for Analysis, Scientific computing and Applications
Department of Mathematics and Computer Science
Eindhoven University of Technology
P.O. Box 513
5600 MB Eindhoven, The Netherlands
ISSN: 0926-4507

Derivative-based image quality measure

for autofocus in electron microscopy

M.E.Rudnaya
R.M.M.Mattheij
J.M.L.Maubach

Abstract Automatic focusing methods are based on an image quality measure, which is a real-valued estimation of an image's sharpness. In this paper we study L_1- or L_2-norm derivative-based image quality measures. For a bench mark case these measures turn out to be quadratic, which implies that after obtaining of at least three images one can find the position of the optimal defocus. The resulting autofocus method is demonstrated for a reference scanning transmission electron microscopy application.

Keywords Electron microscopy · Autofocus · Linear image formation · Image quality measure

1 Introduction

Consider an optical device, such as photocamera, telescope, microscope. An image f depends on a given specimen's geometry f_0 and optical device parameters $\mathbf{p}$

$$f_0, \mathbf{p} \mapsto f.$$

The specimen's geometry is generally unknown. One of the optical device's parameters is the defocus d. The method of automatic determining d, such that the image f has the highest possible quality (the image is *in-focus*), is known as *automated focusing* or *autofocus* method.

The existing autofocus methods used for different types of optical devices are usually based on an Image Quality Measure (IQM)

$$f \mapsto r,$$

a real-valued estimation of an image's sharpness. For a through-focus series the ideal IQM reaches a single optimum (maximum or minimum depending on IQM definition) for the in-focus image. Existing IQMs can be divided into five groups, viz. based on the image derivatives [1,13,27], variance [3,17], autocorrelation [6,14, 24,25], histogram [8,28] or Fourier transform [2,19,23]. An overview of existing IQMs can be found in [10,19,20,28]. An autofocus method can be established in two different ways:

- An amount of images is taken within a wide defocus range and the IQM optimum is determined (course focusing). Next, the same procedure is repeated within the smaller defocus range around the optimum, found on the previous step (fine focusing).
- A search method is used (for example, Fibbonachi search [10,28], Nelder-Mead[17] or Powell interpolation-based trust-region method [18]).

The first approach requires recording of about 20-30 images, which can be time-consuming for real-world applications. The goal of the second approach is to minimize the amount of images necessary to perform the autofocus. The disadvantage of this approach is that it requests an almost perfect (convex) IQM's shape, which is often not the case in real-world applications. The IQM can be noisy (have a lot of minima and maxima). In this case a search method often ends up in one of the local maxima, which can be far away from the actual in-focus position.

A number of IQMs were considered and discussed for different optical devices, such as photographic and video cameras [4,8], telescopes [12], different types of light microscopes [1,6, 10,20,22,27,28] and electron microscopes [2,3, 14,16,19,23]. In this paper we use electron microscopy as a reference application, in particular scanning transmission electron microscopy (STEM).

We study derivative-based IQMs. The advantage of using these measures has been shown

M. E. Rudnaya
Department of Mathematics and Computer Science
Eindhoven University of Technology
Den Dolech 2, 5612AZ, Eindhoven, The Netherlands
Tel.: +31-40-247-31-62
Fax: +31 40-244-24-89
E-mail: m.rudnaya@tue.nl

experimentally for scanning electron microscopy images [16,19]. Some of them are based on L_1- or L_2-norm of an image derivative [1,8,28]. These measures used to be heuristic. Usually they are based on the assumption that the in-focus image has a larger difference between neighboring pixels than the defocused one. In this paper we show analytically how L_1- or L_2-norm derivative-based IQM can be beneficial for a bench mark case of a Gaussian point spread function and a Gaussian object. Numerical computations are performed for the case of a STEM aberration-based point spread function and a STEM experimental microscopic object. The numerically obtained IQM is found to be easily parameterized with a quadratic function just as for the simple bench mark case of a Gaussian object and a Gaussian point spread function. The proposed quadratic parametrization leads to a new autofocus method that requires recording of at least three images only. The method is demonstrated for a real-world microscopy application.

Subsection 1.1 of this paper describes electron microscopy and its challenges for autofocus methods. Subsection 1.2 explains notation and conventions. Section 2 gives an introduction to the linear image formation model. It describes two approximations of STEM point spread function: a Gaussian approximation and an approximation based on microscope's aberrations. In Section 3 we define the L_1- and L_2-norm derivative-based IQMs for one spatial dimension and two spatial dimensions. Four lemmas are introduced, which demonstrate IQM's shape for the simple case of a Gaussian object and a Gaussian point spread function. Based on these shapes the choice for L_1-norm IQM is made. Further discretization of this IQM is presented. Section 4 gives details of numerical computations. Section 5 presents a new autofocus method based on shape-assumptions. Section 6 describes an example of proposed method's work on a real microscope. Section 7 provides discussion and conclusions.

1.1 Electron microscopy

Electron microscopy is a powerful tool in semiconductor industry, life and material sciences. The electron microscope uses electrons instead of photons used in light microscopy. The wavelength of electrons is much smaller than the wavelength of photons, which makes it possible to achieve much higher magnifications.

The simplest Transmission Electron Microscope (TEM) is an analogue of a light microscope. Illumination coming from an electron gun is concentrated on a specimen with a condenser lens. The electrons transmitted through a specimen are focused by an objective lens into a magnified intermediate image, which is enlarged by a projector lenses [5]. In a Scanning Electron Microscope (SEM) a fine probe of electrons is focused at the surface of a specimen and scanned across it. A current of emitted electrons is collected, amplified and used to modulate the brightness of a cathode-ray tube [26]. A Scanning Transmission Electron Microscope is a combination of SEM and TEM. A fine probe of electrons is scanned over a specimen and transmitted electrons are being collected to form an image signal. The resolution in electron microscopy is limited by aberrations of the magnetic lens, but not by the wavelength, as in light microscopy.

The defocus has to be adjusted regularly during the image recording process in the electron microscope. It has to do with regular operations such as inserting a new specimen, changing the stage position or magnification. Other possible reasons are for instance instabilities of the electron microscope or environment and magnetic nature of some specimens. Electron microscopy is a challenging case for an autofocus method. A signal-to-noise ratio in electron microscopy imagery is much worse than in light microscopy. A recording of a single image can be time consuming (especially in STEM), which makes the method much slower. Due to instabilities of environment the image geometry changes in time. Specimen drift and contamination might take place, which makes the method's work more difficult.

1.2 Notation and Conventions

Convolution of two functions $f_1, f_2 \in L_2(\Omega)$ is

$$(f_1 * f_2)(\mathbf{x}) := \int_\Omega f_1(\mathbf{x}')f_2(\mathbf{x}-\mathbf{x}')d\mathbf{x}'.$$

We say $f \in L_2(\Omega)$ is normalized if

$$\int_\Omega f(\mathbf{x})d\mathbf{x} = 1.$$

The L_1- and L_2- norms are

$$\|\mathbf{x} \to f(\mathbf{x})\|_{L_n} := \sqrt[n]{\int_\Omega |f(\mathbf{x})|^n d\mathbf{x}}, \quad n = 1, 2.$$

The spatial coordinates are written as

$x \in \mathcal{R}$,

for one-dimensional case (1-d) and as

$\mathbf{x} := [x, y]^T \in \mathcal{R}^2$

for two-dimensional case (2-d). In 1-d the normalized Gaussian function with standard deviation $|\sigma|$ is

$$g(x, \sigma, \mu) := \frac{1}{\sqrt{2\pi}|\sigma|} e^{-\frac{(x-\mu)^2}{2\sigma^2}}, \quad \sigma \neq 0.$$

The 2-d analogous is

$$G(\mathbf{x}, \boldsymbol{\sigma}, \boldsymbol{\mu}) := g(x, \sigma_x, \mu_x) g(y, \sigma_y, \mu_y), \tag{1}$$

where $\boldsymbol{\sigma} := [\sigma_x, \sigma_y]^T$, $\boldsymbol{\mu} := [\mu_x, \mu_y]^T$.

2 Modelling

Let

$$f_0(x) \in L_2(\mathcal{R}), \quad f_0(x) \geq 0. \tag{2}$$

be the 1-d object function that describes a specimen's geometry image. Due to the linear image formation model [3,7] the microscope's image is a function

$$f(x, \mathbf{p}) = (f_0(x) * h(x, \mathbf{p}))(x) + \epsilon(x), \tag{3}$$

where $\mathbf{p} \in \mathcal{R}^m$ is a vector of microscope's parameters, h is a normalized Point Spread Function (PSF) that describes electron or light beam, ϵ is additive noise. The function h is generally unknown. In 2-d the object function that describes a specimen's geometry image is

$$F_0(\mathbf{x}) \in L_2(\mathcal{R}^2), \quad F_0(\mathbf{x}) \geq 0. \tag{4}$$

Due to the linear image formation model [3,7] the microscope's image is a function

$$F(\mathbf{x}, \mathbf{p}) = (F_0(\mathbf{x}) * H(\mathbf{x}, \mathbf{p}))(\mathbf{x}) + \epsilon(\mathbf{x}), \tag{5}$$

where H is a PSF.

In microscopy PSF is often approximated with a Gaussian function [3,13]. Gaussian standard deviation $|\sigma|$ is proportional to microscope's defocus d. The smaller $|\sigma|$ is the better the image f describes the object f_0. Ideally, if we assume $\sigma = 0$, Gaussian PSF becomes a delta function and $f = f_0$. However, in the real-world situation the PSF standard deviation is bounded by microscopes physical limits $\sigma = \sigma_{min} > 0$. In electron microscopy $\sigma_x \neq \sigma_y$ in (1) if astigmatism aberration is present [3]; $\sigma_x = \sigma_y = \sigma$ corresponds to astigmatism-free situation, which is usually the case in light microscopy [13].

A Gaussian PSF is a rough approximation of a microscope's PSF, which is, however, easier to use for analytical computations. Further we give an overview of a classical alternative, more accurate model [7]. In Section 4 this model is used for numerical computations.

The wave function that enters the specimen is given in a frequency space by assuming a fully coherent point source of electrons in the far field

$$B(\mathbf{u}, \mathbf{p}) = A(\mathbf{u}) e^{-\mathrm{i}\chi(\mathbf{u}, \mathbf{p})}, \tag{6}$$

where $\mathbf{u} = [u, v]^T$ are frequency coordinates. Here the aperture function A is

$$A(\mathbf{u}) := \begin{cases} 1, \text{ if } |\mathbf{u}| \leq q_0 \\ 0, \text{ elswise,} \end{cases} \tag{7}$$

and the wave aberration function χ is defined as in [7]

$$\chi(\mathbf{u}, \mathbf{p}) := \pi\lambda|\mathbf{u}|^2 \times \tag{8}$$

$$(d + \frac{1}{2}\lambda^2|\mathbf{u}|^2 C_s + C_a \cos(2(\phi - \phi_a))),$$

where $\lambda, d, C_s, C_a, \phi_a$ represent the wavelength, the defocus, the spherical aberration, the two-fold astigmatism amplitude and the two-fold astigmatism rotation angle respectively. The electron wavelength λ is related to the electron energy E, the speed of light c and the electron's rest mass m_0 [7]

$$\lambda = \frac{hc}{\sqrt{E(2mc^2 + E)}}. \tag{9}$$

The aperture radius q_0 in (7) controls the convergence semi angle α_0 of the beam by

$$q_0 := \frac{\alpha_0}{\lambda}. \tag{10}$$

The PSF is the intensity of a scanning probe, that is the inverse Fourier transform of the wave function (6)

$$h(\mathbf{x}, \mathbf{p}) = C\left|\mathfrak{F}^{-1}[B]\right|^2, \tag{11}$$

where C is a normalization constant (h is normalized). The conditions when the image reaches

its highest quality are known as Scherzer conditions [21]. For incoherent image formation they are given in [7] as

$$q_{Sh} := \frac{1}{\lambda}(\frac{6\lambda}{C_s})^{\frac{1}{4}}, \tag{12}$$

$$d_{Sh} := -(1.5C_s\lambda)^{1/2}. \tag{13}$$

The tolerable defocus error is defined as in [2]

$$d_e := \sqrt{(\frac{w}{2})^2 + (\frac{t}{2})^2},$$

where t is the specimen's thickness and w is the depth of field defined in [5] as

$$w := \frac{\delta}{\alpha}$$

for the pixel width δ. We consider the tolerable defocus error as the lower bound set by the depth of field

$$d_e = \frac{\delta}{2\alpha}. \tag{14}$$

3 Image Quality Measure

In this section we provide four lemmas, that correspond to 1-d or 2-d and $L1-$ or $L2-$norm derivative-based IQMs. While in real life the image is always a function in 2-d we provide definitions and lemmas for 1-d, in order to achieve a better understanding of IQM's behavior. The proofs of all lemmas in this section are given in the appendix. The lemmas assume noise-free image formation, i.e. $\epsilon = 0$ in (3) and (5).

In 1-d we define the L_1-norm derivative-based IQM

$$r_1(\mathbf{p}) := \frac{1}{s_1^2(\mathbf{p})}, \tag{15}$$

where

$$s_1(\mathbf{p}) := \|x \to \partial_x f(x, \mathbf{p})\|_{L_1}.$$

Lemma 1 *In 1-d for a Gaussian object function*

$f_0(x) = g(x, \sigma_s, \mu_s)$

and for a Gaussian PSF for $\mathbf{p} = \sigma$

$h(x, \sigma) = g(x, \sigma, 0)$

the IQM (15) is

$$r_1(\sigma) = \frac{\pi}{2}(\sigma^2 + \sigma_s^2). \tag{16}$$

In Lemma 1 we show that the IQM is proportional to the PSF standard deviations. It means that for the fixed object geometry ($\sigma_s =$ const) IQM reaches its minimum for the in-focus image (image obtained for $\sigma = \sigma_{min}$). Also, it changes monotonically according to $|\sigma|$. Thus, it satisfies properties of ideal IQM for the bench mark case of a Gaussian PSF and a Gaussian object. It is important to note that IQM also depends on σ_s. It shows that IQM values are always comparative but not absolute, i.e. if we shift the microscope stage without changing microscopic parameters $\mathbf{p}$ and investigate a Gaussian particle with a different width $\sigma_s' \neq \sigma_s$ the IQM values will be different. This is one of the reasons why in real-world applications one obtains a number of images in order to find IQM optimum for a given specimen's area, instead of using the knowledge about IQM optimal values from the different specimen areas.

In 1-d we define L_2-norm derivative-based IQM

$$r_2(\mathbf{p}) := \frac{1}{s_2^{3/2}(\mathbf{p})}, \tag{17}$$

where

$$s_2(\mathbf{p}) := \|x \to \partial_x f(x, \mathbf{p})\|_{L_2}^2.$$

Lemma 2 *In 1-d for a Gaussian object function*

$f_0(x) = g(x, \sigma_s, \mu_s)$

and for a Gaussian PSF for $\mathbf{p} = \sigma$

$h(x, \sigma) = g(x, \sigma, 0)$

the IQM (17) is

$$r_2(\sigma) = 2(2\pi)^{\frac{1}{3}}(\sigma^2 + \sigma_s^2).$$

In 2-d we define L_1-norm derivative-based IQM

$$R_1(\mathbf{p}) := \frac{1}{S_{x,1}^2(\mathbf{p})} + \frac{1}{S_{y,1}^2(\mathbf{p})}. \tag{18}$$

where

$$S_{x,1}(\mathbf{p}) := \|\mathbf{x} \to \partial_x F(\mathbf{x}, \mathbf{p})\|_{L_1}, \tag{19}$$

$$S_{y,1}(\mathbf{p}) := \|\mathbf{x} \to \partial_y F(\mathbf{x}, \mathbf{p})\|_{L_1}. \tag{20}$$

Lemma 3 *In 2-d for a Gaussian object function with* $\boldsymbol{\sigma}_s := [\sigma_{x,s}, \sigma_{y,s}]^T$ *and* $\boldsymbol{\mu}_s := [\mu_{x,s}, \mu_{y,s}]^T$

$$F_0(\mathbf{x}) = G(\mathbf{x}, \boldsymbol{\sigma}_s, \boldsymbol{\mu}_s)$$

and for a Gaussian PSF for $\mathbf{p} = \boldsymbol{\sigma} := [\sigma_x, \sigma_y]^T$

$$H(\mathbf{x}, \boldsymbol{\sigma}) = G(\mathbf{x}, \boldsymbol{\sigma}, 0)$$

the derivative-based IQM (18) is

$$R_1(\boldsymbol{\sigma}) = \frac{\pi}{2}(\sigma_x^2 + \sigma_y^2 + \sigma_{s,x}^2 + \sigma_{s,y}^2).$$

In STEM astigmatism aberration of magnetic lens leads to $\sigma_x \neq \sigma_y$. For astigmatism-free case $\sigma_x = \sigma_y = \sigma$, thus

$$R_1(\sigma) = \frac{\pi}{2}(2\sigma^2 + \sigma_{x,s}^2 + \sigma_{y,s}^2). \tag{21}$$

In 2-d we define L_2-norm derivative-based IQM

$$R_2(\mathbf{p}) := \frac{1}{S_{x,2}^2(\mathbf{p})} + \frac{1}{S_{y,2}^2(\mathbf{p})}. \tag{22}$$

where

$$S_{x,2}(\mathbf{p}) := \|\mathbf{x} \to \partial_x F(\mathbf{x}, \mathbf{p})\|_{L_2}^2,$$

$$S_{y,2}(\mathbf{p}) := \|\mathbf{x} \to \partial_y F(\mathbf{x}, \mathbf{p})\|_{L_2}^2.$$

Lemma 4 *In 2-d for a Gaussian object function with* $\boldsymbol{\sigma}_s := [\sigma_{s,x}, \sigma_{s,y}]^T$ *and* $\boldsymbol{\mu}_s := [\mu_{s,x}, \mu_{s,y}]^T$

$$F_0(\mathbf{x}) = G(\mathbf{x}, \boldsymbol{\sigma}_s, \boldsymbol{\mu}_s)$$

and for a Gaussian PSF for $\mathbf{p} = \boldsymbol{\sigma} := [\sigma_x, \sigma_y]^T$

$$H(\mathbf{x}, \boldsymbol{\sigma}) = G(\mathbf{x}, \boldsymbol{\sigma}, 0)$$

the derivative-based image quality measure (22) is

$$R_2(\boldsymbol{\sigma}) = 64\pi^2(\sigma_x + \sigma_{s,x})(\sigma_y + \sigma_{s,y}) \times ((\sigma_x + \sigma_{s,x})^2 + (\sigma_y + \sigma_{s,y})^2).$$

For astigmatism-free case $\sigma_x = \sigma_y = \sigma$, thus

$$R_2(\boldsymbol{\sigma}) = 64\pi^2(\sigma + \sigma_{s,x})(\sigma + \sigma_{s,y}) \times ((\sigma + \sigma_{s,x})^2 + (\sigma + \sigma_{s,y})^2). \tag{23}$$

In numerical computations of Section 4 we focus at the L_1-norm derivative-based IQM (21), because it can be represented as a quadratic function of PSF standard deviation. This simplifies the situation in comparison with L_2-norm IQM, which is shown to be the fourth order polynomial of PSF standard deviation (23). In the following subsection we explain discretization of L_1-norm derivative-based IQM (18).

3.1 IQM discretization

In real-world applications the recorded images are always discrete. In this subsection we discuss how to compute L_1-norm derivative-based IQM for discrete images. In the remain we neglect the vector of microscope's parameters in the notation of the image, i.e. we use $\mathbf{x} \to F(\mathbf{x})$ instead of $(\mathbf{x}, \mathbf{p}) \to F(\mathbf{x}, \mathbf{p})$ in (5). Also, we use S_x, S_y, R instead of $S_{x,1}, S_{y,1}, R_1$ in (18)-(20).

Let image domain be given as

$$\mathbb{X} := [x_{min}, x_{max}] \times [y_{min}, y_{max}],$$

which means

$$F(\mathbf{x}) = 0, \quad \forall \mathbf{x} \notin \mathbb{X}.$$

We consider an $N \times M$ piecewise constant equisized pixel discretization of $\mathbb{X}$ with pixel dimensions

$$\delta_x := \frac{x_{max} - x_{min}}{N}, \quad \delta_y := \frac{y_{max} - y_{min}}{M}.$$

For most real-world applications the pixel dimensions are equal $\delta = \delta_x = \delta_y$. The discretization of the image domain for $x_i - x_{i-1} = \delta_x, \quad y_i - y_{i-1} = \delta_y$ is

$$x_{min} + \frac{\delta}{2} = x_1 < \ldots < x_n = x_{max} - \frac{\delta}{2}, \tag{24}$$

$$y_{min} + \frac{\delta}{2} = y_1 < \ldots < y_n = y_{max} - \frac{\delta}{2}. \tag{25}$$

For $i \in \{1, \ldots, N\}, \quad j \in \{1, \ldots, M\}$ we define

$$F_{i,j} := F(x_i, y_j). \tag{26}$$

The microscopy images are discrete images that can be represented by a matrix

$$\mathbf{F} = ((F_{i,j})_{i=1}^N)_{j=1}^M. \tag{27}$$

We approximate the image derivative

$$\left|\frac{\partial F}{\partial x}(x, y)\right| \doteq \left|\frac{F(x + \Delta x, y) - F(x, y)}{\Delta x}\right|.$$

Let $\Delta x = k\delta_x, \quad k \in \mathcal{N}$, then

$$\left|\frac{\partial F}{\partial x}(x_i, y_j)\right| \doteq \frac{1}{(k\delta_x)}|F_{i+k,j} - F_{i,j}|.$$

We approximate IQM with the Riemann sum

$$S_x \doteq \sum_{i,j} \delta_x \delta_y \frac{1}{k\delta_x}|F_{i+k,j} - F_{i,j}|,$$

or the discrete IQM is defined

$$\bar{S}_x := \frac{\delta}{k} \sum_{i,j} |F_{i+k,j} - F_{i,j}|, \tag{28}$$

Table 1 Summarization of numerical computations with a Gaussian object and a Gaussian PSF.

Computation N	Pixel difference k	Noise amplitude ϵ_{max}
1.	1	0
2.	1	0.001
3.	3	0.001
4.	30	0.001

$$\bar{S}_y := \frac{\delta}{k} \sum_{i,j} |F_{i,j+k} - F_{i,j}|, \tag{29}$$

$$\bar{R} := \frac{1}{\bar{S}_x^2} + \frac{1}{\bar{S}_y^2}. \tag{30}$$

Analogically in 1-d

$$\bar{s} := \frac{1}{k} \sum_{i} |f_{i+k} - f_i|, \tag{31}$$

$$\bar{r} := \frac{1}{\bar{s}^2}. \tag{32}$$

If we ignore $\frac{\delta}{k}$ in front of the sum and set *pixel difference parameter* $k = 1$, the formula (28) coincides with derivative-based IQM definition in [8,28], known as *Absolute gradient sharpness measure*. In this paper we use (30) instead in order to obtain quadratic parametrization of IQM. Parameter k in (28) can be adjusted to make the IQM less noise-sensitive. In the case of very noisy imaginary it can be used in combination with image denoising techniques, such as [11,15] or [9].

4 Numerical computations

In this section we describe three numerical computations: 1) Numerically computed IQMs for the bench mark case of a Gaussian object and a Gaussian PSF are compared with analytical observations of Section 3 with and without adding noise; 2) Numerically computed IQMs of real microscopic object image and aberration-based PSF described in Section 2 are accurately parameterized with quadratic curve; 3) IQMs of experimental STEM focus series with different pixel difference parameter k are computed and discussed.

4.1 Numerical computations for a Gaussian object and a Gaussian PSF

We consider a Gaussian object in 1-d with standard deviation $\sigma_s = 0.5$. The image domain

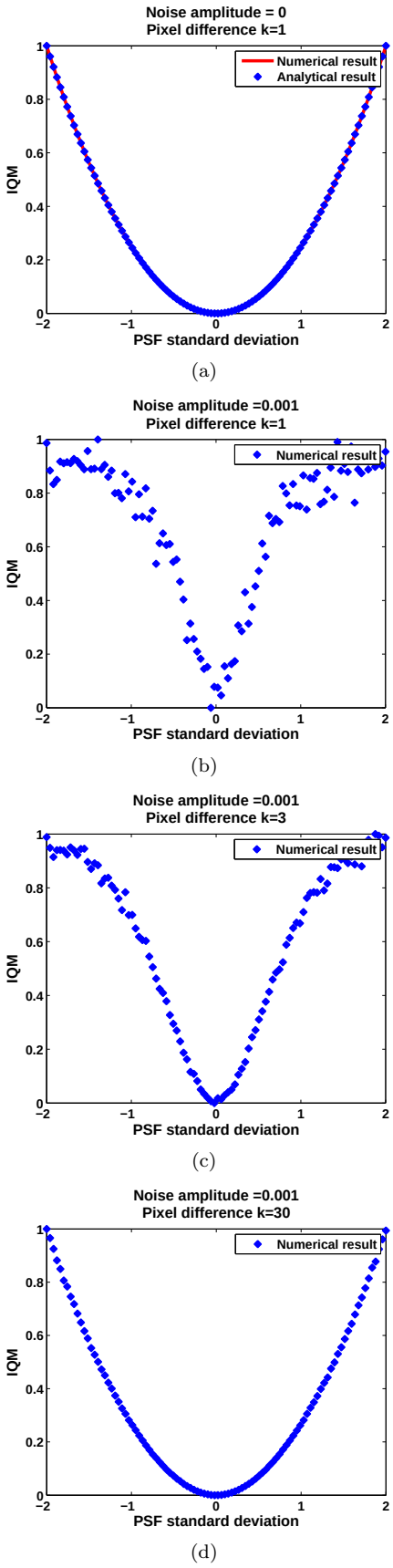

Fig. 1 Numerical computations of IQMs for a Gaussian object and a Gaussian PSF in 1-d.

Fig. 2 Numerically computed STEM PSFs for different defocus values.

Table 2 Parameter values used for numerical computations.

Notation	Parameter	Physical Value
C_s	Spherical aberration	1.07 mm
E	Electron energy	300 keV
λ	Electron wavelength	1.9×10^{-2} nm
q_{Sh}	Scherzer aperture	5.3 nm
d_{Sh}	Scherzer defocus	-55.2 nm
α_0	Semi angle	10.2 mrad
d_e	Tolerable error	9.2 nm

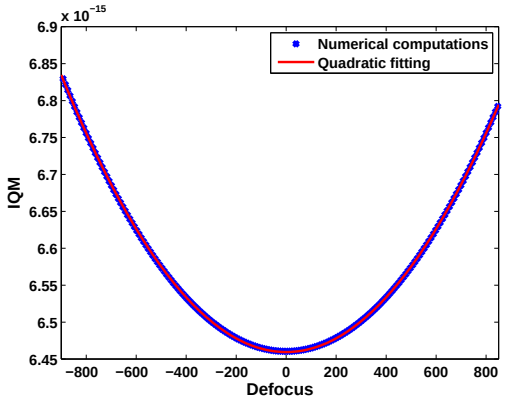

Fig. 3 IQM for STEM image of carbon cross grating and aberration-based PSF is fitted with quadratic function.

$\mathbb{X} = [-10, 10]$ is discretized for $N = 10000$ data points. We consider Gaussian PSF standard deviation $\sigma \in [-2; 2]$. Totally 100 1-d images are computed numerically according to the linear image formation model (3) for σ changing within the given interval. For every image IQM is computed according to (32).

We consider a white additive noise in linear image formation (3) with an amplitude ϵ_{max}. Totally four numerical computations are performed for different values of pixel difference parameter k and ϵ_{max}. The values are summarized in Table 1. The results of four computations are shown in Figure 1.

In the first computation IQM is estimated via (16) as well. Figure 1(a) shows IQM computed numerically and analytically. Numerical and analytical values coincide with the least squares difference of only 2.62×10^{-8}. The noise amplitude $\epsilon_{max} = 0$, and IQM has a perfect quadratic shape.

In the second computation the noise amplitude $\epsilon_{max} = 0.001$. The resulting IQM is shown in Figure 1(b). As a consequence of the noise presence in the images the IQM function becomes noisy as well (it has a lot of local minima and maxima). A local optimum search method, such as Fibbonachi search [10, 28], Nelder-Mead [17] or Powell interpolation-based trust-region method [18], might have difficulties in finding the global optimum of such a function. Also, the IQM function changes its shape: It does not look like quadratic, but like a Gaussian. Increasing the value of k in the third computation reduces the noise amplitude in IQM. However, that Gaussian shape is still present. In the last computation k is increased further, and the IQM has a perfect quadratic shape.

4.2 Numerical computations for a microscopic object image and an aberration-based PSF

In the second computation experimental in-focus STEM image of carbon cross grating is used as an object function. The carbon cross-grating specimen is designed for microscope calibration. The example of carbon cross grating STEM image is shown in Figure 4. The computed PSF is based on the aberration model described in Section 2. For the computation the realistic physical values listed in Table 2 are used. We consider astigmatism-free situation $C_a = 0$. A few numerically computed PSFs for different defocus values are shown in Figure 2. The IQM is computed for images obtained according to linear image formation model (5) for the noise-free situation $\epsilon = 0$. In order to speed up the computations the convolution is carried out in the Fourier space

$$F = \mathfrak{F}^{-1}[\mathfrak{F}[F_0]\mathfrak{F}[H]]. \tag{33}$$

In (33) $\mathfrak{F}$ denotes fourier transform and $\mathfrak{F}^{-1}$ denotes inverse fourier transform. Figure 3 shows

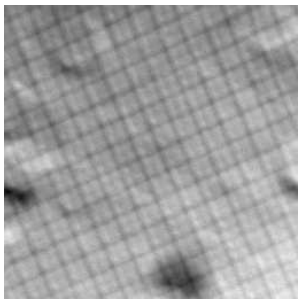

(a) Defocus = -16 μm

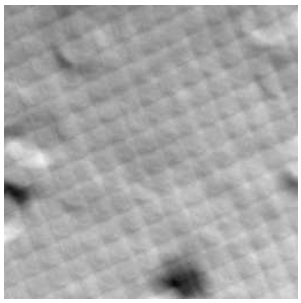

(b) Defocus = -14 μm

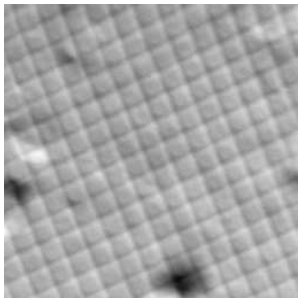

(c) Defocus = -12 μm

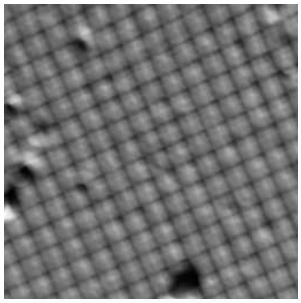

(d) Defocus = -4 μm

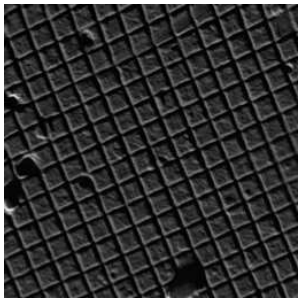

(e) Defocus = 0 μm

Fig. 4 Images from experimental focus series obtained at magnification 10000×.

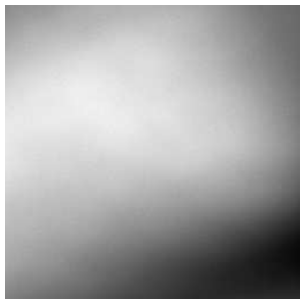

(a) Defocus = -2.35 μm

(b) Defocus = -1.45 μm

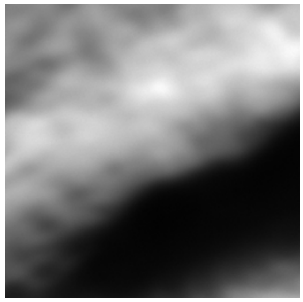

(c) Defocus = -0.45 μm

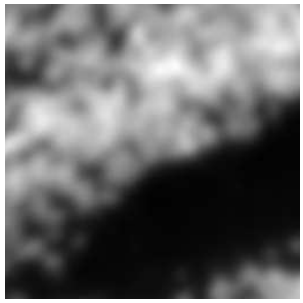

(d) Defocus = -0.05 μm

Fig. 5 Images from experimental focus series obtained at magnification 100000×.

computed IQM. IQM reaches its minimum at the position of Scherzer defocus (13). The numerically obtained IQM can be accurately fitted with the quadratic function, though the object function deviates from a Gaussian object and the PSF deviates from a Gaussian PSF.

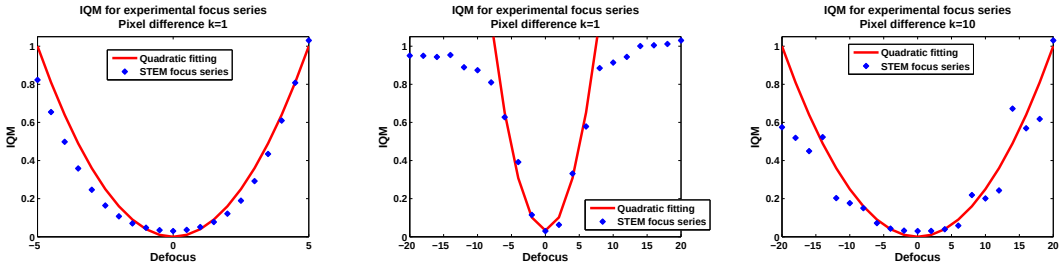

(a) (b) (c)

Fig. 6 IQMs for experimental microscopic focus series fitted with quadratic curves.

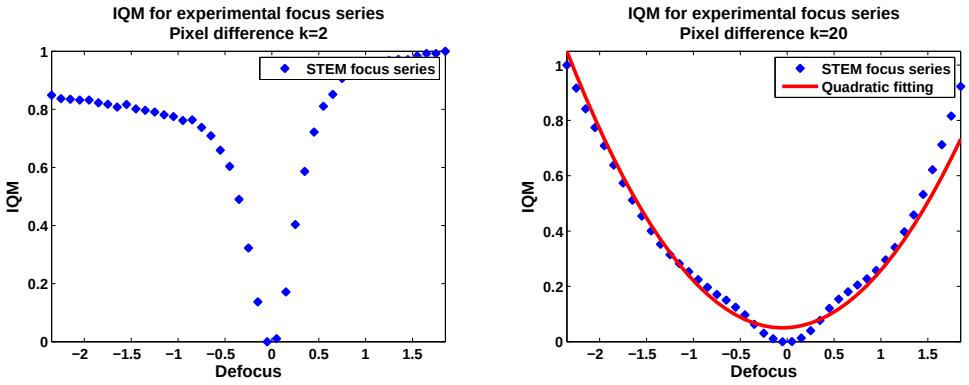

Fig. 7 IQMs for experimental microscopic focus series for pixel difference $k = 2$ and $k = 20$ fitted with quadratic curves for.

4.3 Numerical computations for STEM through-focus series

For numerical computations in this subsection we use three experimental STEM focus series of carbon cross-grating images. The first two series are obtained at the magnification of 10000×. The series are recorded for two different defocus intervals of $[-5; 5]$ μm (fine focus series) and $[-20; 20]$ μm (course focus series). Each series consists of 21 images. Some examples of these images are shown in Figure 4.

The computed IQMs for the two series are shown in Figure 6(a) and Figure 6(b). The pixel difference parameter $k = 1$. The IQM of the fine series is accurately fitted with a quadratic curve (Figure 6(a)), while the IQM of the course series behaves differently than a quadratic curve outside the interval of $[-5; 5]$ μm (Figure 6(b)). It has a Gaussian behavior similar to one observed in numerical computations of Subsection 4.1 (Figure 1). Because the images are obtained from a real-world machine they are definitely effected by noise, which could be one of the reasons for such a behavior. Further we compute IQM for the course series with $k = 10$. The result is shown in Figure 6(c). The shape is closer to quadratic curve, but still single data points have unstable behavior. This behavior deals with the nature of the images in the series. For instance, observing three images obtained at $-16, -14, -12$ μm (Figure 4) we see that the image at -14 μm has less details then images at -16 and -12 μm, i.e. it looks less sharp. As a consequence IQM has a local maximum at -14 μm (Figure 6(c)). This phenomenon could be explained by the fact that far away from ideal defocus some other details of the specimen (probably, from different specimen heights) become visible. For example, the image at -16 μm has some details that the other images in the figure do not have: We can observe small spots in the crosses of the grids and some variations at the surface levels. This type of phenomena can also deal with specimen, environment or machine instabilities, such as instabilities of electron beam.

Further the IQM is computed for experimental cross-grating focus series obtained at magnification 100000×. The images examples are shown in Figure 5. According to (14) at the higher magnifications the image quality is more sensitive to the change of defocus parameter. We can see that the image at only -2.35 μm

defocus is totally out of focus. The IQMs for different pixel difference parameter values are shown in Figure 7. Behavior similar to one in the previous computation takes place. We observe that increasing pixel difference parameter k leads to quadratic shape of IQM.

5 Autofocus method

In Section 2, Lemma 3 we have shown that for certain assumptions the derivative-base IQM can be expressed as

$$R(\sigma) = \frac{\pi}{2}(2\sigma^2 + \sigma_{s,x}^2 + \sigma_{s,y}^2).$$

In general, the standard deviation σ of a PSF can be expressed as a linear function of the machine defocus d. This means that the derivative-base IQM can be parameterized as a quadratic curve with three unknown parameters $[\tilde{a}, \tilde{b}, \tilde{c}]^T$

$$R(d) = \tilde{a}(d - \tilde{c})^2 + \tilde{b}. \tag{34}$$

The numerical computations of Section 4 show that this observation might also hold for real-world microscopic objects and PSFs different from Gaussians. Assume, we have obtained three microscopic images with defocus values d_1, d_2, d_3. The values of IQMs computed for the three images are R_1, R_2, R_3 correspondingly. Parametrization (34) leads to attempt to estimate the ideal defocus position $d = \tilde{c}$ from the three data points

$$\begin{cases} R_1 = \tilde{a}(d_1 - \tilde{c})^2 + \tilde{b} \\ R_2 = \tilde{a}(d_2 - \tilde{c})^2 + \tilde{b} \\ R_3 = \tilde{a}(d_3 - \tilde{c})^2 + \tilde{b} \end{cases} \Rightarrow$$

$$\tilde{c} = \frac{1}{2}\frac{\frac{d_2^2 - d_1^2}{R_2 - R_1} - \frac{d_3^2 - d_2^2}{R_3 - R_2}}{\frac{d_2 - d_1}{R_2 - R_1} - \frac{d_3 - d_2}{R_3 - R_2}}. \tag{35}$$

The above observation leads to an algorithm for a new autofocus method:

1. Choose $\Delta d \gg d_e$.
2. Compute

   $R_1 := R(d_1)$

   for the current microscope state d_1 and for two other microscope states $d_2 = d_1 - \Delta d < d_1 < d_1 + \Delta d = d_3$
3. We estimate a new point $d = \tilde{c}$ according to (35).
4. For $d_4 = d$ we compute

   $R_4 := R(d_4)$.

   We set $n = 4$.
5. We fit n given points with a curve of three parameters (34). For this purpose the linear regression can be used. For

   $R(d) = \beta_0 + \beta_1 d + \beta_2 d^2$

   we consider

   $$\underbrace{\begin{pmatrix} 1 & d_1 & d_1^2 \\ \dots & \dots & \dots \\ 1 & d_n & d_n^2 \end{pmatrix}}_{\mathbf{P}} \underbrace{\begin{pmatrix} \beta_0 \\ \beta_1 \\ \beta_2 \end{pmatrix}}_{\boldsymbol{\beta}} = \underbrace{\begin{pmatrix} R_1 \\ \dots \\ R_n \end{pmatrix}}_{\mathbf{R}}.$$

   By means of projection

   $\mathbf{P}^T\mathbf{P}\boldsymbol{\beta} = \mathbf{P}^T\mathbf{R}$

   we obtain a linear system of three equations with three unknowns, compute $\boldsymbol{\beta}$ and obtain $d_{n+1} = \tilde{c}_{n+1}$.
6. If $|\tilde{c}_n - \tilde{c}_{n+1}| < d_e$, stop. Elsewise $R_{n+1} = R(\tilde{c}_{n+1})$ and go to the previous step.

The last three steps of the algorithm are optional. They are required mainly if very accurate focusing is needed. The main goal of this paper is to try to estimate the in-focus image position from three preliminary obtained images (steps 1-3). Experiments with the method are presented in the following section.

6 Real-world application

The method is implemented in a prototype FEI Tecnai F20 STEM. One example of an application run is shown in Figure 8. The initial position of the machine defocus is $d_1 = -3$ μm, which corresponds to the left lower image in Figure 8. The defocus step $\Delta d = 5$ μm is chosen. The two intermediate images with $d_2 = d_1 - \Delta d = -8$ μm and $d_3 = d_1 + \Delta d = 2$ μm are obtained (upper raw of Figure 8). The position of the in-focus image is computed from the given three images with (35) and corresponds to $d_4 = 0.3$ μm, which is within the defocus error for the given machine settings. The improvements of the image quality are visible in Figure 8.

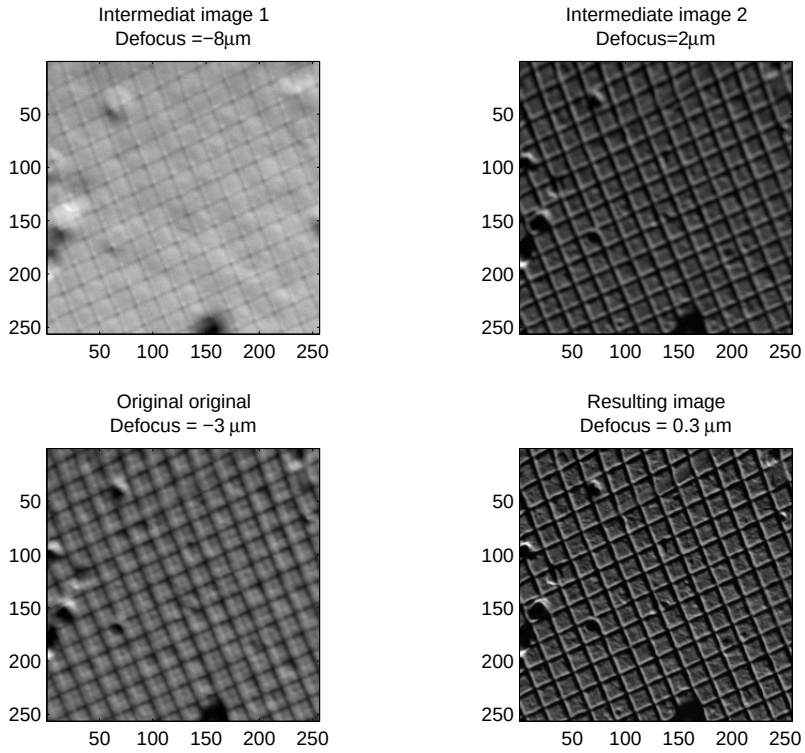

Fig. 8 Image improvement by a test application implemented in a prototype FEI Tecnai F20 STEM.

7 Discussion and conclusions

This paper proposes IQM-based autofocus method that requires recording of only at least three images, while standard autofocus technique requires recording of about 10-15 images. The method is applied to a STEM reference case. The method is based on a specific but general enough assumption on the shape of IQM, so that it can be used for other types of optical devices. The work of the method depends on the choice of input parameters, such as initial defocus value d_1, defocus shift Δd and pixel difference k. Considering $\sigma_x \neq \sigma_y$ and a parameterized quadratic function in two-parameter space the method could be extended for the purpose of simultaneous autofocus and two-fold astigmatism correction in electron microscopy.

Appendix - proofs of lemmas

Derivatives of a Gaussian function in 1-d

$$\partial g(x,\sigma,\mu) = -\frac{(x-\mu)}{\sigma^2} g(x,\sigma,\mu). \tag{36}$$

and in 2-d

$$\partial_x G(x,\boldsymbol{\sigma},\boldsymbol{\mu}) = -\frac{(x-\mu_x)}{\sigma_x^2} G(x,\boldsymbol{\sigma},\boldsymbol{\mu}),$$

$$\partial_y G(y,\boldsymbol{\sigma},\boldsymbol{\mu}) = -\frac{(y-\mu_y)}{\sigma_y^2} G(y,\boldsymbol{\sigma},\boldsymbol{\mu}). \tag{37}$$

The convolution of two Gaussian function is a Gaussian again:

$$(g(x,\sigma_1,\mu_1) * g(x,\sigma_2,\mu_2))(x) =$$

$$g(x, \sqrt{\sigma_1^2+\sigma_2^2}, \mu_1+\mu_2). \tag{38}$$

The integrals similar to a Gaussian integral are

$$\int_0^\infty x^{2n} e^{-\frac{x^2}{a^2}} dx = \sqrt{\pi}\frac{2n!}{n!}(\frac{a}{2})^{2n+1},$$

$$\int_0^\infty x^{2n+1} e^{-\frac{x^2}{a^2}} dx = \frac{n!}{2} a^{2n+2}, \quad n \in \mathbb{N}. \tag{39}$$

Lemma 1 *In 1-d for a Gaussian object function*

$$f_0(x) = g(x,\sigma_s,\mu_s)$$

and for a Gaussian PSF for $\mathbf{p} = \sigma$

$$h(x,\sigma) = g(x,\sigma,0)$$

the IQM (15) is

$$r_1(\sigma) = \frac{\pi}{2}(\sigma^2 + \sigma_s^2).$$

Proof According to linear image formation model (3) and (38) we obtain

$$f = g(x, \sqrt{\sigma^2 + \sigma_s^2}, \mu_s).$$

Then the absolute value of the image derivative is

$$|\partial_x f| = \frac{|x - \mu_s|}{\sigma^2 + \sigma_s^2} g(x, \sqrt{\sigma^2 + \sigma_s^2}, \mu_s).$$

Further the L_1-norm of the image derivative is

$$s_1(\sigma) = \int_{-\infty}^{+\infty} |\partial_x f| dx =$$

$$\int_{-\infty}^{+\infty} \frac{|x - \mu_s|}{\sqrt{\sigma^2 + \sigma_s^2}} g(x, \sqrt{\sigma^2 + \sigma_s^2}, \mu_s) dx =$$

$$\frac{1}{\sqrt{2\pi}(\sigma^2 + \sigma_s^2)^{\frac{3}{2}}} (- \int_{-\infty}^{\mu_s} (x - \mu_s) e^{-\frac{(x-\mu_s)^2}{2(\sigma^2+\sigma_s^2)}} dx +$$

$$\int_{\mu_s}^{+\infty} (x - \mu_s) e^{-\frac{(x-\mu_s)^2}{2(\sigma^2+\sigma_s^2)}} dx).$$

Substitute $x' = \frac{(x-\mu_s)^2}{2(\sigma^2+\sigma_s^2)} \Rightarrow dx' = \frac{(x-mu_1)}{\sigma^2+\sigma_s^2} dx$, then

$$s_1(\sigma) = \frac{1}{\sqrt{2\pi}(\sigma^2 + \sigma_s^2)^{\frac{3}{2}}} (\sigma^2 + \sigma_s^2) \times$$

$$(- \int_{+\infty}^{0} e^{-x'} dx' + \int_{0}^{+\infty} e^{-x'} dx')$$

or

$$s_1(\sigma) = \frac{\sqrt{2}}{\sqrt{\pi(\sigma^2 + \sigma_s^2)}},$$

and as a consequence

$$r_1(\sigma) := \frac{1}{s_1^2(\sigma)} = \frac{\pi}{2}(\sigma^2 + \sigma_s^2).$$

Lemma 2 *In 1-d for a Gaussian object function*

$$f_0(x) = g(x, \sigma_s, \mu_s)$$

and for a Gaussian PSF for $\mathbf{p} = \sigma$

$$h(x, \sigma) = g(x, \sigma, 0)$$

the IQM (17) is

$$r_2(\sigma) = 2(2\pi)^{\frac{1}{3}}(\sigma^2 + \sigma_s^2).$$

Proof Analogically to Lemma 1

$$(\partial_x f)^2 = \frac{(x - \mu_s)^2}{(\sigma^2 + \sigma_s^2)^2} g^2(x, \sqrt{\sigma^2 + \sigma_s^2}, \mu_s),$$

which leads to

$$s_2(\sigma) := \int_{-\infty}^{+\infty} (\partial_x f)^2 dx =$$

$$\int_{-\infty}^{+\infty} \frac{(x - \mu_s)^2}{(\sigma^2 + \sigma_s^2)^2} g^2(x, \sqrt{\sigma^2 + \sigma_s^2}, \mu_s) dx =$$

$$\frac{1}{2\pi(\sigma^2 + \sigma_s^2)^3} \int_{-\infty}^{\infty} (x - \mu_s)^2 e^{-\frac{(x-\mu_s)^2}{\sigma^2+\sigma_s^2}} dx =$$

$$\frac{1}{\pi(\sigma^2 + \sigma_s^2)^3} \int_{0}^{\infty} x^2 e^{-\frac{x^2}{\sigma^2+\sigma_s^2}} dx.$$

Then according to (39)

$$s_2(\sigma) = \frac{1}{4\sqrt{\pi}(\sigma^2 + \sigma_s^2)^{\frac{3}{2}}},$$

thus

$$r_2(\sigma) := \frac{1}{s_2^{2/3}(\mathbf{p})} = 2(2\pi)^{\frac{1}{3}}(\sigma^2 + \sigma_s^2).$$

Lemma 3 *In 2-d for a Gaussian object function with* $\boldsymbol{\sigma}_s := [\sigma_{x,s}, \sigma_{y,s}]^T$ *and* $\boldsymbol{\mu}_s := [\mu_{x,s}, \mu_{y,s}]^T$

$$F_0(\mathbf{x}) = G(\mathbf{x}, \boldsymbol{\sigma}_s, \boldsymbol{\mu}_s)$$

and for a Gaussian PSF for $\mathbf{p} = \boldsymbol{\sigma} := [\sigma_x, \sigma_y]^T$

$$H(\mathbf{x}, \boldsymbol{\sigma}) = G(\mathbf{x}, \boldsymbol{\sigma}, 0)$$

the derivative-based IQM (18) is

$$R_1(\boldsymbol{\sigma}) = \frac{\pi}{2}(\sigma_x^2 + \sigma_y^2 + \sigma_{s,x}^2 + \sigma_{s,y}^2).$$

Proof According to the linear image formation model

$$F(\mathbf{x}, \boldsymbol{\sigma}) = \iint_{\mathcal{R}^2} G(\mathbf{x}', \boldsymbol{\sigma}) G(\mathbf{x} - \mathbf{x}', \boldsymbol{\sigma}, \boldsymbol{\mu}) d\mathbf{x}' =$$

$$\Big(g(x, \sigma_x, 0) * g(x, \sigma_{s,x}, \mu_{s,x})\Big)(x) \times$$

$$\Big(g(y, \sigma_y, 0) * g(y, \sigma_{s,y}, \mu_{s,y})\Big)(y) =$$

$$g(x, \sqrt{\sigma_x^2 + \sigma_{s,x}^2}, \mu_{s,x}) g(y, \sqrt{\sigma_y^2 + \sigma_{s,y}^2}, \mu_{s,y}).$$

Then the absolute values of 2-d image derivatives

$$|\partial_x F| = \frac{|x - \mu_{s,x}|}{\sigma_x^2 + \sigma_{s,x}^2} g(x, \sqrt{\sigma_x^2 + \sigma_{s,x}^2}, \mu_{s,x}) \times$$

$$g(y, \sqrt{\sigma_y^2 + \sigma_{s,y}^2}, \mu_{s,y}),$$

$$|\partial_y F| = \frac{|y-\mu_{s,y}|}{\sigma_y^2+\sigma_{s,y}^2} g(x, \sqrt{\sigma_x^2+\sigma_{s,x}^2}, \mu_{s,x}) \times$$

$$g(y, \sqrt{\sigma_y^2+\sigma_{s,y}^2}, \mu_{s,y}),$$

and as a consequence from Lemma 1

$$S_{x,1}(\sigma_x, \sigma_y) = s(\sigma_x) \int_{\mathcal{R}} g(y, \sqrt{\sigma_y^2+\sigma_{s,y}^2}, \mu_{s,y}) dy$$

$$S_{y,1}(\sigma_x, \sigma_y) = s(\sigma_y) \int_{\mathcal{R}} g(x, \sqrt{\sigma_x^2+\sigma_{s,x}^2}, \mu_{s,x}) dx$$

or

$$S_{x,1}(\boldsymbol{\sigma}) = s(\sigma_x) = \frac{\sqrt{2}}{\sqrt{\pi(\sigma_x^2+\sigma_{s,x}^2)}},$$

$$S_{y,1}(\boldsymbol{\sigma}) = s(\sigma_y) = \frac{\sqrt{2}}{\sqrt{\pi(\sigma_y^2+\sigma_{s,y}^2)}},$$

then

$$R(\boldsymbol{\sigma}) := \frac{1}{S_{x,1}^2(\boldsymbol{\sigma})} + \frac{1}{S_{y,1}^2(\boldsymbol{\sigma})} =$$

$$= \frac{\pi}{2}(\sigma_x^2+\sigma_y^2+\sigma_{s,x}^2+\sigma_{s,y}^2).$$

Lemma 4 *In 2-d for a Gaussian object function with* $\boldsymbol{\sigma}_s := [\sigma_{s,x}, \sigma_{s,y}]^T$ *and* $\boldsymbol{\mu}_s := [\mu_{s,x}, \mu_{s,y}]^T$

$$F_0(\mathbf{x}) = G(\mathbf{x}, \boldsymbol{\sigma}_s, \boldsymbol{\mu}_s)$$

and for a Gaussian PSF for $\mathbf{p} = \boldsymbol{\sigma} := [\sigma_x, \sigma_y]^T$

$$H(\mathbf{x}, \boldsymbol{\sigma}) = G(\mathbf{x}, \boldsymbol{\sigma}, 0)$$

the derivative-based image quality measure (22) is

$$R_2(\boldsymbol{\sigma}) = 64\pi^2(\sigma_x+\sigma_{s,x})(\sigma_y+\sigma_{s,y}) \times \\ ((\sigma_x+\sigma_{s,x})^2 + (\sigma_y+\sigma_{s,y})^2).$$

Proof Analogically to Lemma 3

$$(\partial_x F)^2 = \frac{(x-\mu_{s,x})^2}{(\sigma_x^2+\sigma_{s,x}^2)^2} g^2(x, \sqrt{\sigma_x^2+\sigma_{s,x}^2}, \mu_{s,x}) \times$$

$$g^2(y, \sqrt{\sigma_y^2+\sigma_{s,y}^2}, \mu_{s,y}),$$

$$(\partial_y F)^2 = \frac{(y-\mu_{s,y})^2}{(\sigma_y^2+\sigma_{s,y}^2)^2} g^2(x, \sqrt{\sigma_x^2+\sigma_{s,x}^2}, \mu_{s,x}) \times$$

$$g^2(y, \sqrt{\sigma_y^2+\sigma_{s,y}^2}, \mu_{s,y}),$$

and as a consequence from Lemma 2

$$S_{x,2}(\sigma_x, \sigma_y) =$$

$$s_2(\sigma_x) \int_{\mathcal{R}} g^2(y, \sqrt{\sigma_y^2+\sigma_{s,y}^2}, \mu_{s,y}) dy =$$

$$\frac{1}{4\sqrt{\pi}(\sigma_x^2+\sigma_{s,x}^2)^{(3/2)}} \cdot \frac{1}{2\sqrt{\pi}\sqrt{\sigma_y^2+\sigma_{s,y}^2}},$$

$$S_{y,2}(\sigma_x, \sigma_y) =$$

$$s_2(\sigma_y) \int_{\mathcal{R}} g^2(x, \sqrt{\sigma_x^2+\sigma_{s,x}^2}, \mu_{s,x}) dx =$$

$$\frac{1}{4\sqrt{\pi}(\sigma_y^2+\sigma_{s,y}^2)^{(3/2)}} \cdot \frac{1}{2\sqrt{\pi}\sqrt{\sigma_x^2+\sigma_{s,x}^2}},$$

then

$$R(\boldsymbol{\sigma}) = \frac{1}{S_{x,2}^2} + \frac{1}{S_{y,2}^2} =$$

$$64\pi^2(\sigma_x+\sigma_{s,x})(\sigma_y+\sigma_{s,y}) \times$$

$$((\sigma_x+\sigma_{s,x})^2 + (\sigma_y+\sigma_{s,y})^2).$$

Acknowledgements We kindly acknowledge R. Doornbos (ESI) for assistance with obtaining experimental data.

This work has been carried out as a part of the Condor project at FEI Company under the responsibilities of the Embedded Systems Institute (ESI). This project is partially supported by the Dutch Ministry of Economic Affairs under the BSIK program.

References

1. Brenner, J., Dew, B., Brian Horton, J., King, T., Neurath, P., Selles, W.: An automated microscope for cytologic research a preliminary evaluation. J. Histochem. Cytochem. **24**(1), 100–111 (1976)
2. Van den Broek, W.: Advanced focus methods in electron microscopy: Tomographic reconstruction of the EELS data cube autofocus of HAADF-STEM images. Ph.D. thesis, University of Antwerp (2007)
3. Erasmus, S., Smith, K.: An automatic focusing and astigmatism correction system for the SEM and CTEM. J. Microsc. **127**(2), 185–199 (1982)
4. Erteza, A.: Sharpness index and its application to focus control. Appl. Opt. **15**(4), 877–881 (1976)
5. Goodhew, P.J., Humphreys, J., Beanland, R.: Electron microscopy and analysis. 3rd ed. edn. London : Taylor & Francis (2001)
6. Hilsenstein, V.: Robust autofocusing for automated microscopy imaging of fluorescently labelled bacteria. In: Proceedings of International Conference on Digital Image Computing: Techniques and Applications (2005)
7. Kirkland, E.J.: Advanced Computing in Electron Microscopy. Plenum Press (1998)
8. Krotkov, E.: Focusing. Int. J. Comput. Vis. **1**, 223–237 (1987)
9. Le, T., Chartrand, R., Asaki, T.: A variational approach to reconstructing images corrupted by poisson noise. J. Math. Imaging Vis. **27**(3), 257–263 (2007)
10. Liu, X., Wang, W., Sun, Y.: Dynamic evaluation of autofocusing for automated microscopic analysis of blood smear and pap smear. J. Microsc. **227**, 15–23 (2007)

11. Morigi, S., Reichel, L., Sgallari, F., Shyshkov, A.: Cascadic multiresolution methods for image deblurring. SIAM J. Imaging Sci. **1**(1), 51–74 (2007)
12. Muller, R., Buffington, A.: Real-time correction of atmospherically degraded telescope images through image sharpening. J. Opt. Soc. Am. **64**(9), 1200–1210 (1974)
13. Nayar, S.K., Nakagawa, Y.: Shape from focus. IEEE Trans. Pattern Anal. Mach. Intell. **16**(8), 824–831 (1994)
14. Ong, K., Phang, J., Thong, J.: A robust focusing and astigmatism correction method for the scanning electron microscope-part II: Autocorrelation-based coarse focusing method. Scanning **20**, 324–334 (1997)
15. Perona, P., Malik, J.: Scale-space and edge detection using anisotropic diffusion. IEEE Trans. Pattern Anal. Mach. Intell. **12**(7), 629–639 (1990)
16. Rudnaya, M., Mattheij, R., Maubach, J.: Iterative autofocus algorithms for scanning electron microscopy. Microsc. Microanal. **15**, 1108–1109 (2009)
17. Rudnaya, M.E., Van den Broek, V., Doornbos, R., Mattheij, R.M.M., Maubach, J.M.L.: Autofocus and two-fold astigmatism correction in HAADF-STEM. Casa-report 10-09, Eindhoven University of Technology (2010)
18. Rudnaya, M.E., Kho, S., Mattheij, R.M.M., Maubach, J.M.L.: Derivative-free optimization for autofocus and astigmatism correction in electron microscopy. In: Proceedings of 2nd International Conference on Engineering Optimization (2010)
19. Rudnaya, M.E., Mattheij, R.M.M., Maubach, J.M.L.: Evaluating sharpness functions for automated scanning electron microscopy. J. Microsc. **in press** (2010)
20. Santos, A., De Solórzano, C.O., Vaquero, J.J., Peña, J.M., Malpica, N., Del Pozo, F.: Evaluation of autofocus functions in molecular cytogenetic analysis. J. Microsc. **188**, 264–272 (1997)
21. Scherzer, O.: The theoretical resolution limit of the electron microscope. J. Appl. Phys. **20**, 20–29 (1949)
22. Sun, Y., Duthaler, S., Nelson, B.: Autofocusing in computer microscopy: Selecting the optimal focus algorithm. Microsc. Res. Tech. **65**, 139–149 (2004)
23. Tanaka, N., Hu, J., Baba, N.: An on-linea correction method of defocus and astigmatism in haadf-stem. Ultamicroscopy **78**, 103–110 (1999)
24. Vollath, D.: Automatic focusing by correlative methods. J. Microsc. **147**, 279–288 (1987)
25. Vollath, D.: The influence of the scene parameters and of noise on the behaviour of automatic focusing algorithms. J. Microsc. **151**, 133–146 (1997)
26. Watt, I.: The principles and practice of electron microscopy. 2nd ed. edn. Cambridge University Press (1997)
27. Yang, G., Nelson, B.: Wavelet-based autofocusing and unsupervised segmentation of microscopic images. In: Proceedings of the Intl. Conference on Intelligent Robots and Systems (2003)
28. Yeo, T., Ong, S., Jayasooriah, Sinniah, R.: Autofocusing for tissue microscopy. Image Vis. Comput. **11**(10), 629–639 (1993)

PREVIOUS PUBLICATIONS IN THIS SERIES:

Number	Author(s)	Title	Month
10-38	A.S. Tijsseling Q. Hou B. Svingen A. Bergant	Acoustic resonance in a reservoir-pipeline-orifice system	July '10
10-39	A. Keramat A.S. Tijsseling A. Ahmadi	Investigation of transient cavitating flow in viscoelastic pipes	July '10
10-40	V. Chalupecký T. Fatima A. Muntean	Multiscale sulfate attack on sewer pipes: Numerical study of a fast micro-macro mass transfer limit	July '10
10-41	E.J.W. ter Maten J. Rommes	Predicting 'parasitic ffects' in large-scale circuits	July '10
10-42	M.E. Rudnaya R.M.M. Mattheij J.M.L. Maubach	Derivative-based image quality measure	July '10

Ontwerp: de Tantes,
Tobias Baanders, CWI